

# Optimal radial basis for density-based atomic representations

Alexander Goscinski,<sup>1</sup> Félix Musil,<sup>1</sup> Sergey Pozdnyakov,<sup>1</sup> and Michele Ceriotti<sup>1, a)</sup>

Laboratory of Computational Science and Modeling, Institute of Materials,  
École Polytechnique Fédérale de Lausanne, 1015 Lausanne, Switzerland

The input of almost every machine learning algorithm targeting the properties of matter at the atomic scale involves a transformation of the list of Cartesian atomic coordinates into a more symmetric representation. Many of these most popular representations can be seen as an expansion of the symmetrized correlations of the atom density, and differ mainly by the choice of basis. Here we discuss how to build an adaptive, optimal numerical basis that is chosen to represent most efficiently the structural diversity of the dataset at hand. For each training dataset, this optimal basis is unique, and can be computed at no additional cost with respect to the primitive basis by approximating it with splines. We demonstrate that this construction yields representations that are accurate and computationally efficient, presenting examples that involve both molecular and condensed-phase machine-learning models.

## I. INTRODUCTION

Machine-learning algorithms for atomistic simulations rely heavily on the transformation of structural information and chemical composition into descriptors, or features.<sup>1–3</sup> An effective molecular representation should be invariant (or more generally, equivariant) with respect to symmetry operations,<sup>3–9</sup> be capable of differentiating between inequivalent configurations,<sup>10</sup> and sensitive to atomic deformations<sup>11,12</sup>. In broad terms it should encode in the most efficient way the relationships between a structure and the properties one is interested in predicting.<sup>13</sup> Even though many alternative approaches have been proposed to construct a representation that fulfils (at least partly) these requirements,<sup>14</sup> it has become clear that many of the existing schemes are strongly connected to each other, and can be seen as projections on different choices of basis functions of the correlations of the atom density<sup>15,16</sup>, or equivalently of a cluster expansion of interactions<sup>17,18</sup>. We bring this insight to its logical conclusion, by showing that an optimal, data-driven basis to expand the atom density can be built as a contraction of a larger primitive basis set (similarly to what is routinely done in quantum chemistry for Gaussian type orbitals<sup>19</sup>) and that it can be practically, and inexpensively, evaluated as a numerical basis (again, with striking similarities to similar ideas in electronic-structure methods<sup>20</sup>). We demonstrate the accuracy, and the computational efficiency, of this approach for both the construction of machine-learning potentials for materials, and for the prediction of molecular properties.

## II. THEORY

We use the bra-ket notation originally introduced in Refs. 15,16, and discussed in detail in Ref. 14. An atomic structure  $A$  is represented in terms of its atom

density

$$\langle a\mathbf{x}|A;\rho\rangle = \sum_i \delta_{aa_i} \langle \mathbf{x}|\mathbf{r}_i;g\rangle, \quad (1)$$

where  $\langle \mathbf{x}|\mathbf{r}_i;g\rangle \equiv g(\mathbf{x} - \mathbf{r}_i)$ , is a Gaussian of width  $\sigma_a$  centered on the position  $\mathbf{r}_i$  of the  $i$ -th atom, and  $a_i$  is an index that indicate the chemical nature of that atom. Translational symmetrization breaks this global atom density into a sum of atom-centred neighbour densities  $|A;\langle \rho^{\otimes 2}\rangle_{\mathbb{R}^3}\rangle = \sum_i |A;\rho_i\rangle$ ,

$$\langle a\mathbf{x}|A;\rho_i\rangle = \sum_{j \in A} \delta_{aa_j} \langle \mathbf{x}|\mathbf{r}_{ji};g\rangle f_{\text{cut}}(r_{ji}), \quad (2)$$

where  $\mathbf{r}_{ji} = \mathbf{r}_j - \mathbf{r}_i$ , and we introduce a smooth cutoff function  $f_{\text{cut}}$  to restrict the range of the environment.

It is convenient to express  $\langle a\mathbf{x}|A;\rho_i\rangle$  on a basis of spherical harmonics  $Y_l^m(\hat{\mathbf{x}}) \equiv \langle \hat{\mathbf{x}}|lm\rangle$  and radial functions  $R_{nl}(x) \equiv \langle x|nl\rangle$ ,

$$\langle anlm|A;\rho_i\rangle = \int d\mathbf{x} \langle nl|x\rangle \langle lm|\hat{\mathbf{x}}\rangle \langle a\mathbf{x}|A;\rho_i\rangle. \quad (3)$$

Regardless of the choice of  $\langle x|nl\rangle$ , one can evaluate the density coefficients as a sum over neighbors

$$\langle anlm|\rho_i\rangle = \sum_j \delta_{aa_j} \langle nl|r_{ji};g\rangle \langle lm|\hat{\mathbf{r}}_{ji}\rangle, \quad (4)$$

where  $\langle nl|r;g\rangle$  is a radial integral

$$\langle nl|r;g\rangle = 4\pi e^{-\frac{r^2}{2\sigma_a^2}} \int_0^\infty dx x^2 \langle nl|x\rangle e^{-\frac{x^2}{2\sigma_a^2}} i_l\left(\frac{xr}{\sigma_a^2}\right), \quad (5)$$

that can be computed analytically for some choices of basis, or approximated numerically and computed as a spline for each radial and angular channel pair<sup>21</sup>. The  $\sigma_a \rightarrow 0$  limit corresponds to a  $\delta$ -like density, and can be evaluated as easily on any discrete basis.

### A. Optimal density basis

In Ref. 22 it has been proposed to use principal component analysis to compute the data-driven contractions of equivariant features that best represent

<sup>a)</sup>Electronic mail: michele.ceriotti@epfl.ch

the variability of a dataset. In combination with an iterative expression to compute density correlations of increasing order, this idea underlies the N-body iterative contraction of equivariant (NICE) frameworks. The procedure can be readily applied to the first-order equivariants – that are equal to the density coefficients. Keeping different chemical species separate, this amounts to computing the rotationally invariant covariance matrix (see SI)

$$C_{nn'}^{al} = \frac{1}{N} \sum_i \sum_m \langle anlm | \rho_i \rangle \langle \rho_i | an'lm \rangle. \quad (6)$$

For each  $(a, l)$  channel, one diagonalizes  $\mathbf{C}^{al} = \mathbf{U}^{al} \mathbf{\Lambda}^{al} (\mathbf{U}^{al})^T$ , and computes the optimal coefficients

$$\langle aqlm; \text{opt} | \rho_i \rangle = \sum_n U_{qn}^{al} \langle anlm | \rho_i \rangle. \quad (7)$$

As we discuss later, it is also possible to mix species in this step, by considering a covariance matrix that couples radial and chemical channels. Note that we compute  $\mathbf{C}^{al}$  without centering the density coefficients. For  $l > 0$ , the mean ought to be zero by symmetry (although it might not be for a finite dataset), and even for the totally symmetric,  $l = 0$  terms, density correlation features are usually computed in a way that is more consistent with the use of non-centered features.

The number of contracted numerical coefficients  $q_{\max}$  can be chosen inspecting the eigenvalues  $\Lambda_q^{al}$ . At first, it might appear that in order to evaluate the contracted basis one has to compute the full set of  $n_{\max}$  coefficients, and this is how the idea was applied in Ref. 22. When combining Eq. (7) with Eq. (4), however, one sees that the contracted coefficients can be evaluated directly

$$\langle aqlm; \text{opt} | \rho_i \rangle = \sum_j \delta_{aa_j} \langle aql; \text{opt} | r_{ji}; g \rangle \langle lm | \hat{\mathbf{r}}_{ji} \rangle, \quad (8)$$

using the contracted radial integrals

$$\langle aql; \text{opt} | r; g \rangle = \sum_n U_{qn}^{al} \langle nl | r; g \rangle, \quad (9)$$

that can be computed over a grid of  $r$  points, approximated with splines, and then evaluated at exactly the same cost as for a spline approximation of the radial integrals of a primitive basis of the same size. Splining does not affect the equivariant behavior of the atom-density features, and introduces minute discrepancies relative to the analytical basis that do not affect the quality of the resulting models. As we shall see, after the spline coefficients have been computed for  $n_{\max} \gg q_{\max}$  the initial choice of basis functions is inconsequential. For a given number of radial functions, and a target data set, the data-driven contracted basis provides the most efficient description of the atom-centred density.

## B. Density correlation features

In the vast majority of applications the density coefficients are not used directly in applications, but are combined to build higher order invariant or equivariant features<sup>3,8,16,18</sup>. For example, the powerspectrum (i.e. SOAP invariant features<sup>3</sup>) can be computed as

$$\langle a_1 n_1; a_2 n_2; l | \overline{\rho_i^{\otimes 2}} \rangle \propto \sum_m \frac{(-1)^m}{\sqrt{2l+1}} \langle a_1 n_1 l m | \rho_i \rangle \times \langle a_2 n_2 l (-m) | \rho_i \rangle, \quad (10)$$

where the density coefficients can be either those obtained from GTO functions truncated at increasing  $n_{\max}$ , or those from an optimal basis containing  $q_{\max}$  terms.

We discuss the general case of “multispectra” in the frame of the N-body iterative construction of equivariant (NICE) features<sup>22</sup>, but analogous considerations apply to similar many-body descriptors such as the atomic cluster expansion (ACE)<sup>18,23</sup> or the moment tensor potential (MTP)<sup>6</sup>, and is likely to be relevant also for covariant neural networks<sup>9,24</sup>. We consider the case of a single chemical species, to keep a notation that is by necessity quite cumbersome as simple as possible, but the generalization is trivial. The NICE iteration increases the body order of features that describe correlations between  $\nu$  neighbors  $\langle Q | \overline{\rho_i^{\otimes \nu}}; \sigma; \lambda \mu \rangle$  ( $Q$  is a generic index that labels the features,  $\lambda, \mu, \sigma$  are indices that describe their behavior with respect to rotations and inversion) by combining lower order features

$$\begin{aligned} \langle Q; n l k | \overline{\rho_i^{\otimes (\nu+1)}}; \sigma; \lambda \mu \rangle &\propto \delta_{s\sigma((-1)^{l+k+\lambda})} \\ &\times \sum_m \langle n | \overline{\rho_i^{\otimes 1}}; l m \rangle \langle Q | \overline{\rho_i^{\otimes \nu}}; s; k(\mu - m) \rangle \\ &\times \langle l m; k(\mu - m) | \lambda \mu \rangle, \end{aligned} \quad (11)$$

using Clebsch-Gordan coefficients  $\langle l m; l' m' | l'' m'' \rangle$  in an expression analogous to the sum of angular momenta. The  $\nu = 1$  equivariants are nothing but the density coefficients

$$\langle n | \overline{\rho_i^{\otimes 1}}; l m \rangle = \langle nl(-m) | \rho_i \rangle, \quad (12)$$

and one can compute invariant descriptors by retaining only the  $\langle Q | \overline{\rho_i^{\otimes \nu}}; 1; 00 \rangle$  terms, using the other components only as computational intermediates.

*a. The multi-spectrum in the optimal radial basis*  
First, we investigate the relation between the multi-spectrum computed in an arbitrary radial basis, and in the optimal basis obtained from the principal com-

ponents of the density coefficients.

$$\begin{aligned}
\langle Q; qlk; \text{opt} | \overline{\rho_i^{\otimes(\nu+1)}}; \sigma; \lambda\mu \rangle &\propto \delta_{s\sigma((-1)^{l+k+\lambda})} \\
&\times \sum_m \langle ql(-m); \text{opt} | \rho_i \rangle \langle Q | \overline{\rho_i^{\otimes\nu}}; s; k(\mu-m) \rangle \\
&\quad \times \langle lm; k(\mu-m) | \lambda\mu \rangle \\
&= \delta_{s\sigma((-1)^{l+k+\lambda})} \sum_m \langle lm; k(\mu-m) | \lambda\mu \rangle \\
&\times \sum_n U_{qn}^l \langle nl(-m) | \rho_i \rangle \langle Q | \overline{\rho_i^{\otimes\nu}}; s; k(\mu-m) \rangle \\
&= \sum_n U_{qn}^l \langle Q; nlk | \overline{\rho_i^{\otimes(\nu+1)}}; \sigma; \lambda\mu \rangle. \quad (13)
\end{aligned}$$

In other terms, the change of basis can be achieved by constructing the multispectrum using the density coefficients in the optimal radial basis, or by applying the transformation to each  $(n_\nu, l_\nu)$  term in the multispectrum computed in the original basis. The transformation of the multi-spectrum is given by a block-diagonal matrix composed of the  $\mathbf{U}^l$ .

*b. Truncation of the multispectrum* Among the consequences of Eq. (13) is the fact that – if the optimal basis is not truncated, so that  $\mathbf{U}^l$  enacts an orthogonal transformation – the change to the optimal basis preserves the magnitude of the multi-spectrum:

$$\begin{aligned}
\sum_{q=1}^{n_{\max}} \left| \langle Q; qlk; \text{opt} | \overline{\rho_i^{\otimes(\nu+1)}}; \sigma; \lambda\mu \rangle \right|^2 \\
= \sum_{n=1}^{n_{\max}} \left| \langle Q; nlk | \overline{\rho_i^{\otimes(\nu+1)}}; \sigma; \lambda\mu \rangle \right|^2. \quad (14)
\end{aligned}$$

More generally, truncating the basis to include  $q_{\max}$  optimized basis functions reduces the norm of the multispectrum by an the same multiplicative factor at each iteration

$$\begin{aligned}
\sum_{q=1}^{q_{\max}} \sum_{lkQ} \sum_{\sigma\lambda\mu} \left| \langle Q; qlk; \text{opt} | \overline{\rho_i^{\otimes(\nu+1)}}; \sigma; \lambda\mu \rangle \right|^2 \\
= \sum_{q=1}^{q_{\max}} \sum_{lm} \left| \langle q | \overline{\rho_i^{\otimes 1}}; lm \rangle \right|^2 \times \sum_{Qskp} \left| \langle Q | \overline{\rho_i^{\otimes\nu}}; s; kp \rangle \right|^2 \quad (15)
\end{aligned}$$

which can be derived exploiting the orthogonality of CG coefficients (see SI). One sees how (if the compound index  $Q$  was expanded to indicate the  $q_\nu l_\nu k_\nu$  terms at each order  $\nu$ ) the norm of the multispectrum can be expanded into a product of terms coming from each order, and the errors introduced by truncation accumulate as a product. As a side-note, the combination of Eqs. (14) and (15) implies that, for each environment, the norm of the  $\nu$ -spectrum should equal the norm of the corresponding 1-spectrum raised to the power  $\nu$  when summing over all the equivariant components. This provides a stringent test to estimate the amount of information that is lost when contracting, subselecting, or truncating the angular momentum of the equivariant components during the iterative construction of high body-order features.

### c. Principal-component basis for multi-spectra

The derivation of (15) applies to each environment  $A_i$  separately, and does not translate exactly into an expression for the retained variance (that involves an expression analogous to Eq. (15), averaged over the training set). A similar issue arises when addressing the question of what is the best radial basis (in terms of variance retained for a given level of truncation) that one can use to apply the NICE iteration for a specific feature  $Q$  and intermediate angular momentum state  $k$ . In building the covariance, we sum over  $(\sigma, \lambda, \mu)$  – i.e. we look for a single transformation that applies to all terms that derive from combinations of  $\langle Q | \overline{\rho_i^{\otimes\nu}}; s; kp \rangle$  with the density coefficients

$$\begin{aligned}
NC_{nn'}^l(\nu; Q; s; k) &= \\
\sum_{i\sigma\lambda\mu} \langle Q; nlk | \overline{\rho_i^{\otimes(\nu+1)}}; \sigma; \lambda\mu \rangle \langle \overline{\rho_i^{\otimes(\nu+1)}}; \sigma; \lambda\mu | Q; n'lk \rangle \\
&= \sum_i \sum_m \langle n | \overline{\rho_i^{\otimes 1}}; lm \rangle \langle \overline{\rho_i^{\otimes 1}}; lm | n' \rangle \\
&\quad \times \sum_p \left| \langle Q | \overline{\rho_i^{\otimes\nu}}; s; kp \rangle \right|^2. \quad (16)
\end{aligned}$$

This expression corresponds to a covariance matrix of the density coefficients which is built by weighting the contribution from each environment by the magnitude of  $\langle Q | \overline{\rho_i^{\otimes\nu}}; s; kp \rangle$ . Thus, the optimal combinations that are determined for  $\nu = 1$  are not necessarily equal to those needed in further iterations. Computing a different radial basis for each NICE iteration would be extremely cumbersome; in what follows, we provide evidence that the basis optimized for the density coefficients provides an effective compression even for the higher-order terms in the multispectrum.

## III. RESULTS

To illustrate the construction and use of an optimal radial basis we present two examples: a general-purpose potential for silicon, based on the training dataset from Ref. 25, and the prediction of atomization energies for the organic molecules from the QM9 dataset<sup>26</sup>. These two examples are complementary: the silicon potential involves a single chemical species, uses forces for training and aims to predict the properties of arbitrary (distorted) configurations; the QM9 energy model involves multiple elements, but only minimum-energy structures, and (despite its limitations) has been widely used as a benchmark of new representations for molecular machine learning.<sup>27</sup>

### A. Convergence of the density expansion

Given that the radial integrals (5) are linear in  $\langle x | nl \rangle$ , one can explicitly visualize the “optimal radial basis” that corresponds to the optimized coefficients

$$\langle x | aql; \text{opt} \rangle \equiv \sum_n U_{qn}^{al} \langle x | nl \rangle. \quad (17)$$

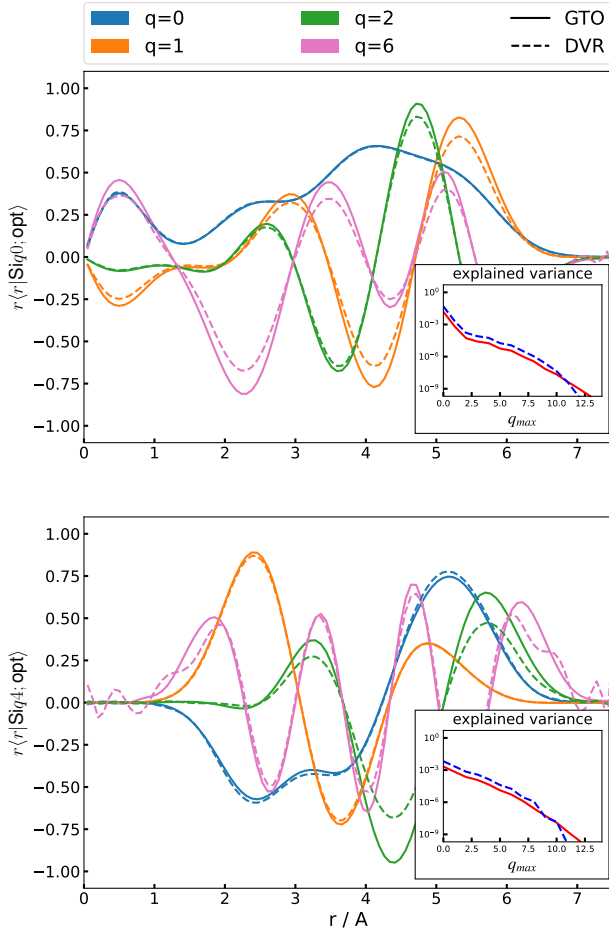


Figure 1: Several examples of the optimized radial basis functions on the silicon dataset for  $l = 0$  and  $l = 4$  using DVR and GTO as primitive basis contracted from  $n_{\max} = 20$ , with  $r_{\text{cut}} = 6$ .

For a given dataset, these functions are optimal in the sense that (a) when truncated to  $q_{\max} < n_{\max}$ , they describe the greatest fraction of the variance for the local atom-density coefficients; (b) they are independent on the choice of the primitive basis, in the limit in which the latter is complete. The optimal functions computed for the Si dataset (Fig. 1) are associated with rapidly decaying covariance eigenvalues. The same radial functions can be obtained starting from either of the DVR or GTO bases implemented in `librascal`: the discrepancy increases for higher indices  $q$ , but can be reduced by increasing the size of the primitive basis, at no cost during the evaluation of the optimal splined basis. Furthermore, the optimal functions reflect some “sensible” expectations – highly oscillating functions are associated with low covariance eigenvalues, the functions decay at the cut-off distance (even if the raw basis exhibits much larger spillover, see SI), and higher angular momentum functions are peaked at larger distances, consistent with the greater variability in the angular distribution at large  $r$ .

In the multi-species case, exemplified by the QM9

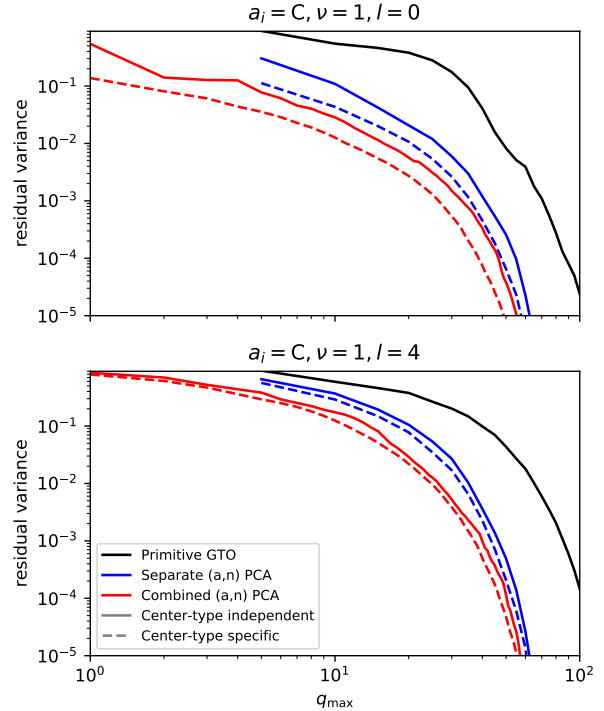


Figure 2: Convergence of the residual variance for the expansion coefficients of the density as a function of the overall size of the, computed for the QM9 dataset and for environments centered on a C atom.

Different series correspond to a GTO basis of increasing size (black), to an optimal basis computed separately for each neighbor density (blue) or by mixing chemical and radial channels ( $a, n$ ) (red). Full lines use the same basis irrespective of the nature of the central atom, dashed lines correspond to a basis optimized specifically for C-centered environments.

dataset, there are several possible choices for the contraction strategy. First, one can compute a different contraction depending on the nature of the central atom, or use the same basis functions independent of  $a_i$ . Second, one can contract separately the density contribution from each neighbour type along the radial index, or compute a covariance matrix that combines the ( $a, n$ ) indices. Figure 2 shows the convergence of the explained variance for the the four possible case, compared to the baseline of a primitive GTO basis of increasing size - which shows by far the slowest convergence of the explained variance, requiring almost 100 radial channels ( $n_{\max} = 20$ , for the 5 species present) to reduce the importance of features below  $10^{-4}$ . The same level can be achieved with  $\approx 50$  channels when performing separate PCAs for each neighbor species, and  $q_{\max} \approx 30$  when computing jointly the correlations between radial and elemental channels. Performing a separate PCA analysis depending on the nature of the central atom accelerates slightly the convergence of the explained variance. It is worth noting that although the NICE code<sup>28</sup> contains the infrastructure to compute these different

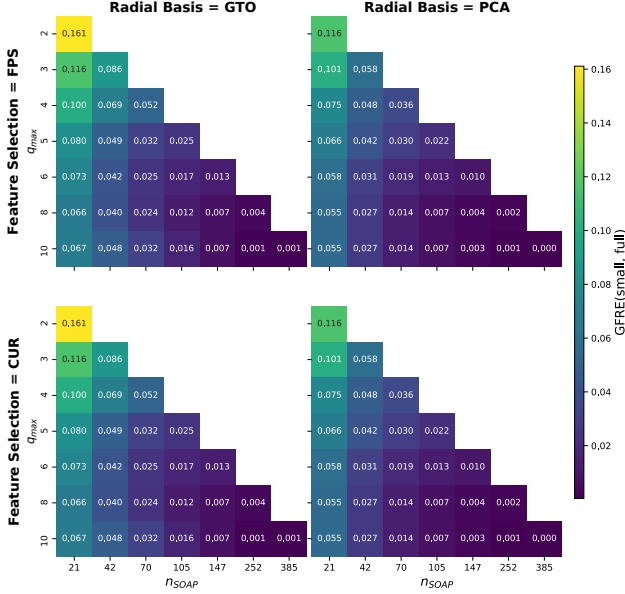


Figure 3: Feature space reconstruction errors for SOAP features, resulting from the truncation of the radial basis and from the selection of a subset of the powerspectrum entries using a deterministic CUR scheme and FPS. The “full” feature space is taken to be SOAP features computed using a GTO basis ( $n_{\max} = 20, l_{\max} = 6$ ), and we compare the convergence obtained by using a smaller GTO basis against a truncated optimal basis of the same size.

kinds of contractions as a *post-processing of the primitive basis*, at present `librascal` only implements the less information-efficient separate PCA strategy. An implementation that evaluates directly the combined contraction would incur an overhead connected with the fact that every neighbor would contribute to every  $q$  channel irrespective of their nature:

$$\begin{aligned}
 \langle qlm; \text{opt} | \rho_i \rangle &= \sum_j \sum_{an} U_{q;an}^l \langle nlm | \mathbf{r}_{ji}; g \rangle \delta_{aa_j} \\
 &= \sum_j \sum_n U_{q;a_j n}^l \langle nl | r_{ji}; g \rangle \langle lm | \hat{\mathbf{r}}_{ji} \rangle \\
 &= \sum_j \langle a_j ql; \text{opt} | r_{ji}; g \rangle \langle lm | \hat{\mathbf{r}}_{ji} \rangle. \quad (18)
 \end{aligned}$$

Given however that the cost of evaluating the density coefficients is usually a small part of the calculation of density-correlation features<sup>21</sup>, we expect that this approach should be preferable to a two-step procedure.

## B. Convergence of density correlations features

We now turn to considering how the truncation of the density expansion basis affects the evaluation of higher-order features, focusing in particular on the invariant components. We begin analyzing the convergence of the powerspectrum computed for the Si dataset. We take the SOAP vector computed with a

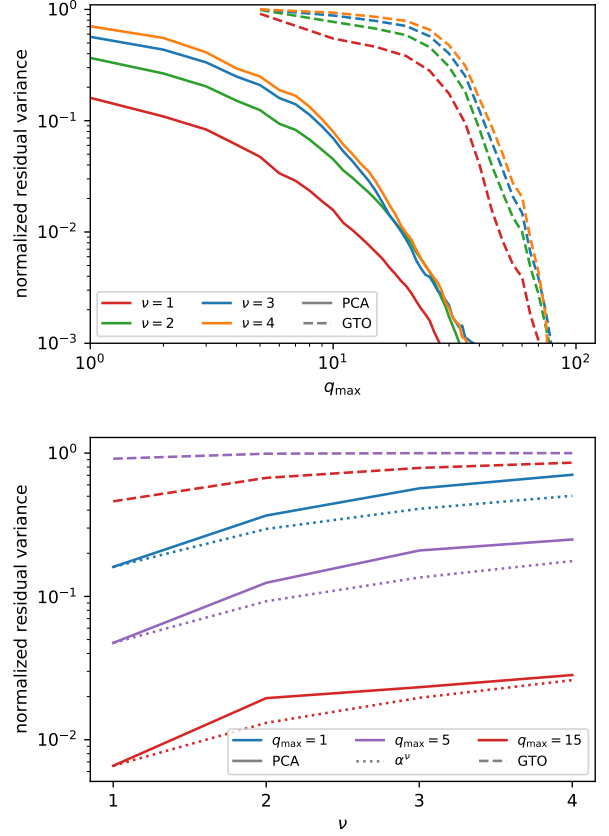


Figure 4: Normalized residual variance (the variance of the feature vector computed for a given  $q_{\max}$  divided by the variance of that computed for the “full” vector  $n_{\max} = 20, l_{\max} = 5$ ). We compare results for a small GTO basis (dashed lines) against those for a center-type specific, species and alpha channel combined optimal density basis. (top) Different colors correspond to order- $\nu$  multispectra.  $\nu = 1$  and  $\nu = 2$  terms are computed in full; for the  $\nu > 2$  terms the NICE contraction has been converged so that the discarded variance at each iteration is smaller than that due to the truncation of the density coefficients. (bottom) Comparison of the residual variance for fixed radial/chemical basis size and different orders of multispectrum. Dotted lines indicate the behavior one would expect if the retained variance followed exactly the multiplicative behavior given in Eq. (15).

large  $n_{\max} = 20$  as the “full” description of three-body correlations, and compute the global feature space reconstruction error<sup>29</sup> (GFRE) that measures how accurately the full feature space can be reconstructed using SOAP features that are built from a truncated density expansion, and further subselected using a low-rank matrix approximation (CUR) approach<sup>30</sup> and farthest point sampling (FPS).<sup>31,32</sup> Using an optimal density expansion basis systematically improves the GFRE compared to a GTO basis of the same size (Figure 3). This is true both for the full-sized SOAP vector, and also for a subselection of the invariant powerspectrum

entries based on a deterministic CUR algorithm, as well as on FPS. This suggests that using an optimal radial basis as the building block of higher-order spectra yields feature vectors that can be easily compressed further. For a fixed number of selected SOAP features, the GFRE decreases monotonically with increasing values of  $q_{\max}$ .

The same efficient compression is observed for the QM9 dataset, when extending the construction to higher-order features and to a multi-component system. Despite the fact that, as discussed in Section II B, there is no formal guarantee that the optimal density coefficients are also optimal to build high- $\nu$  equivariants, we find in practice that the PCA basis leads to much faster convergence of the bispectrum and the trispectrum compared to the primitive basis (Fig. 4, top panel). As shown in the bottom panel of Fig. 4, the truncation of the density coefficients affects the multispectra in a way that is qualitatively similar to what predicted by Eq. (15): the impact of an incomplete description of the density gets amplified by taking successive orders of correlation. Given that the raw number of multispectrum components grows exponentially as  $q_{\max}^\nu$ , the density basis truncation has a dramatic effect in reducing the size of the multispectrum vector. This observation may be extremely important in the construction of systematic high-body order expansions such as NICE or ACE, and in particular in the extension of these approaches to multiple chemical species. The very efficient compression that can be achieved by combining  $(a, n)$  channels at the density level shall make it much easier to avoid the exponential increase of complexity of high-body order models with growing chemical diversity.

### C. Regression models

The construction we discuss guarantees the most effective variance-preserving compression of the density coefficients and – at least approximately – the equivariant features built based on them. There is however no guarantee that the features are the most effective to predict a given target property. In fact, it has already been shown that SOAP features tend to emphasize correlations between atoms that are far from the atomic center, which can lead to a counter-intuitive degradation of the model accuracy with increasing cutoff radius<sup>15,33</sup>. This effect can be contrasted by introducing a radial scaling<sup>13,15</sup> that de-emphasizes the magnitude of the atom density in the region far from the central atom. By applying this scaling – or other analogous tweaks<sup>34</sup> – to the atom density before it is expanded in the primitive basis, one ensures that the optimal basis is also built with a similar focus on the structural features that contribute more strongly to the target property.

The accuracy of a Gaussian approximation potential based on SOAP features, trained using both energy and forces (details in the SI) shows an improvement of the cross-validation error for the most aggres-

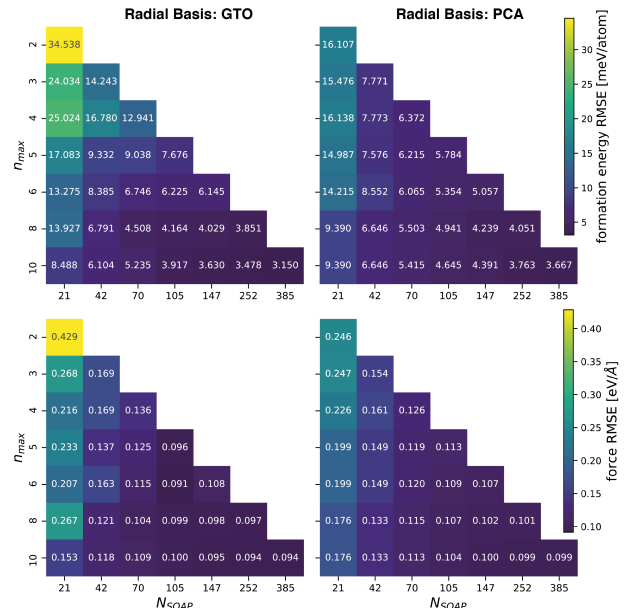


Figure 5: Energy and force RMSE for a Gaussian approximation potential based on the power spectrum, fitted to the Si dataset, plotted as a function of the number of radial functions  $n_{\max}$  and sparsification of the SOAP features,  $n_{\text{SOAP}}$  (using CUR selection).

sive truncation of the feature space (up to  $n_{\max} \approx 6$  for forces, and  $n_{\max} \approx 4$  for energy), but no improvements for large  $n_{\max}$ . For the largest feature set the primitive GTO basis can be up to 10% more accurate than the corresponding optimal-basis model. A comparison with Fig. 3, that shows that the PCA basis is objectively more informative than the primitive basis, suggests that an effect similar to the degradation of performance with increasing environment cutoff radius might be at play here: for this dataset size, the GTO basis (which becomes smoother for large distances) is better suited to build a potential with limited amounts of training data. The fact that the GTO basis may be fortuitously better adapted to this specific regression problem is also suggested by the non-monotonic convergence of the error. Depending on the value of  $n_{\max}$ , the GTO functions are distributed so as to span the  $[0, r_c]$  range (see SI). Particularly for small  $n_{\max}$ , the varying positions of maxima and nodes of the orthogonalized GTOs emphasise different portions of the atomic environment. This can produce such a non-monotonic trend, particularly in the limit of a relatively small train set size. The PCA basis, on the other hand, is constructed to provide a progressively more complete description of the atom density for the specific training set, resulting in a more regular, mostly monotonic convergence.

These effects can be investigated more easily by considering a 2-body model, that uses only the  $\langle n | \rho_i^{\otimes 1} \rangle \propto \langle n 00 | \rho_i \rangle$  features. The comparison between the GTO and the DVR basis (the former being vastly superior in terms of linearly decodable information content<sup>29</sup>)

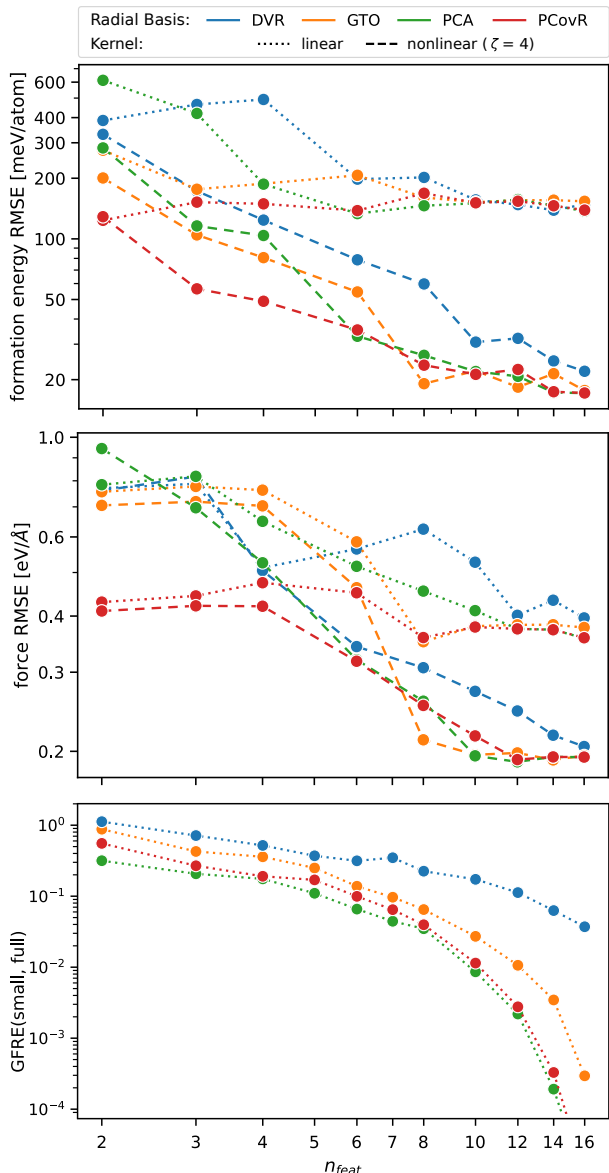


Figure 6: Energy (top) and force (center) 5-fold cross-validation RMSE and GFRE (bottom), computed on the silicon dataset for models based on the radial spectrum  $|\rho_i^{\otimes 1}\rangle$ , as a function of the number of radial functions. Different curves correspond to a primitive DVR and GTO basis, and to the optimal (PCA and PCovR) contracted bases. The PCovR contraction is performed by a 1:9 weighting of the variance and energy prediction losses. Full lines correspond to a linear model, and dashed lines to a polynomial kernel with exponent  $\zeta = 4$ . The GFRE is computed relative to  $n_{\max} = 20$  GTO features.

is far from clear-cut, with GTOs giving the worst results for forces with  $n_{\max} = 4, 6$ . The optimal PCA basis is usually comparable with - but not substantially better than - the best result between GTO and DVRs, for each size of the basis. The relative performance of different basis sets is similar when using a

linear model and a polynomial kernel, although the non-linear model reaches an accuracy that is approximately 6 times better for energies and two times better for forces.

An interesting possibility to extend the scheme we propose here is to incorporate a supervised component in the selection of the optimal basis. Principal covariates regression (PCovR)<sup>35,36</sup> is a simple linear scheme that can be tuned to provide a projection of features to a low-dimensional latent space that combines an optimal variance compression target with that of providing an accurate linear approximation of the desired target property. We can use it easily to determine the contraction coefficients of the basis: as shown in Fig. 6 (center, bottom), this PCovR optimal basis yields much better accuracy in the small  $q_{\max}$  limit. In fact, by taking the “pure regression” limit of PCovR, one would obtain a basis that, for a linear model, yields an accuracy comparable to a fully-converged 2-body potential: in fact, the expansion coefficients for this bespoke radial functions are proportional to the linear regression prediction, and can be evaluated at no additional cost thanks to the spline approximation of the optimal basis. The use of a non-linear model based on the same radial-spectrum features provides the simplest test of transferability for the PCovR-optimized basis. Even though for very small  $q_{\max}$  there is a noticeable improvement (up to a factor of 2 for the force RMSE and  $q_{\max} = 2$ ) against primitive and PCA-optimized bases, the advantage is quickly lost for larger bases, where the variance reduction plays the leading role in driving the selection of radial basis even for small  $\alpha$ . As shown in Fig. 6 (bottom), the improved regression accuracy of PCovR-optimized basis functions comes at a necessary cost in terms of variance reconstruction - even though with an intermediate value of the mixing parameter they achieve higher information content than either of the primitive bases, as measured by the GFRE. A systematic investigation of the effect of varying the parameters of PCovR, as well as the use of PCov-style feature selection<sup>37</sup> in the construction of the multi-spectra, is a promising direction for further research. One of the potential challenges is that it is only meaningful to apply the linear reasoning that underlie PCovR to optimize features with the same equivariant properties as the targets, and so only the  $l = 0$  channel of the density coefficients can be optimized with this scheme.

The advantages of using an optimized radial basis become much clearer for the QM9 dataset. As shown in Fig. 7, there is a dramatic improvement of performance at all body orders when using a PCA-contracted  $(a, n)$  basis, with the improvement becoming more and more substantial for higher  $\nu$ . For bispectrum features and  $q_{\max} = 5$  (effectively only one channel per species) the use of a combined basis leads to a 5-fold reduction of test error compared to the use of a primitive GTO basis, and makes it possible to reach the symbolic threshold of 1 kcal/mol MAE. For larger basis sets, and for  $\nu > 3$ , it becomes necessary to truncate aggressively the construction of multispec-

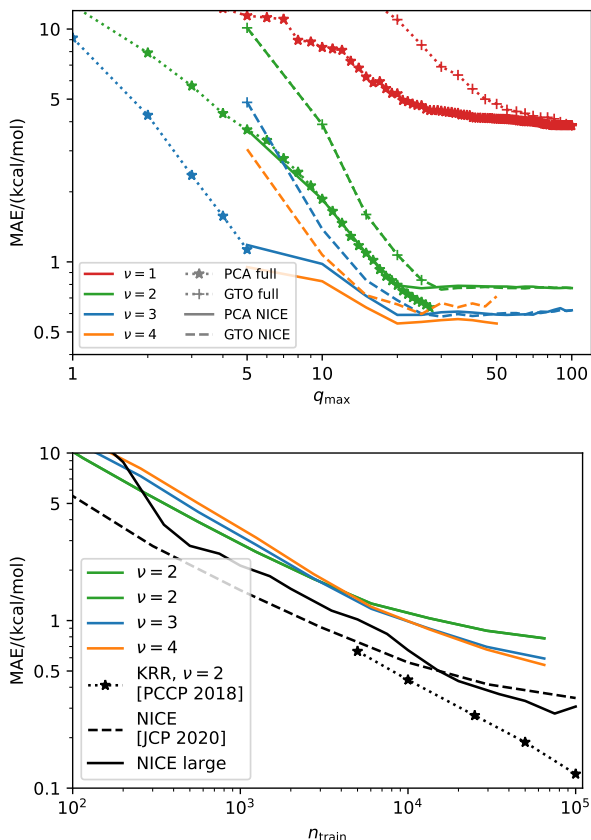


Figure 7: Convergence of ML models of the atomization energy of molecules from the QM9 dataset. (top) convergence as a function of the  $(a, n)$  radial basis size, comparing a primitive GTO basis and an optimal PCA contraction, for different body orders of the features. For large  $q_{\max}$  it is necessary to truncate aggressively the NICE iteration, which reduces the limiting accuracy of the model. All curves are for a training set containing 65’000 structures. (bottom) Learning curves for linear models built on PCA optimal features of increasing body order. All curves are computed with  $q_{\max} = 50$ . The figure also shows results for a kernel model based on the powerspectrum, using parameters analogous to those in Ref. 15, for the NICE model from Ref. 22, and for a large NICE model with 53390 features.

tra, which within the current implementation of the NICE framework is achieved with the help of some thresholding heuristics. In order to be able to use a consistent threshold up to the full primitive GTO basis (which contains  $n_{\max} = 20$  radial terms per chemical species) we need to use a rather aggressive scheme, which results in clear performance loss, as evidenced by the saturation of the model accuracy with increasing  $q_{\max}$ .

The interplay of the truncation of the density coefficients, the thresholding heuristics, and the use of the features in a linear or a non-linear model, is evident in the lower panel of Fig. 7, which compares NICE

models computed with  $q_{\max} = 50$  and aggressive truncation of the body-order iteration, with the more balanced settings from Ref. 22 ( $n_{\max} = 12$ ,  $l_{\max} = 7$ ,  $\nu_{\max} = 5$ , 1000 invariant features per body order), with a “large NICE” model which includes 53880 features (up to  $\nu = 4$ , built upon a relatively small spherical expansion with  $l_{\max} = 5$  and  $n_{\max} = 5$ ), and with a kernel ridge regression model that uses the same parameters as in Ref. 15 (i.e. using only the power spectrum and a non-linear kernel). The details of the NICE construction affect substantially the stability and the accuracy of the model in the high- $n_{\text{train}}$  limit, that vary by a factor of two. Furthermore, a non-linear model based on low-body order features is the most accurate, and reaching a state-of-the-art MAE of 0.12kcal/mol with  $n_{\text{train}} = 10^5$ . Even though a thorough investigation of these aspects is beyond the scope of the present investigation, the understanding of the interplay between the truncation of the density basis and the information loss at higher body order that we discuss here shall support more systematic studies in the future.

#### IV. CONCLUSIONS

Most of the widely adopted representations for machine learning of atomistic properties can be seen as a discretization of the correlations of the atom density. This realization naturally points to the importance of determining the most expressive and concise basis to expand the atom density. For a given dataset it is possible to define uniquely a basis that is optimal in terms of its ability to linearly compress the information encoded in the variance of the density coefficients, which can be determined as a contraction of any complete primitive basis, and evaluated efficiently by approximating it with splines. We have explored, both analytically and with numerical experiments, the implications of this choice to evaluate higher-order correlations of the density, and to build linear and non-linear regression models of the energy of both condensed-phase silicon and small organic molecules.

Our study indicates that the optimization of the density basis has a dramatic impact on the information content of higher-order features, but that - particularly for comparatively small training sets - achieving the ultimate accuracy also requires tuning the basis, or the underlying atomic density, to reflect the sensitivity of the target property to changes in the atomic configurations. From this point of view, the construction of an “unsupervised” optimal basis makes it possible to perform this tuning at the level of the atomic density, which is usually more intuitive than a tuning of the basis. For instance, one can reduce the weight and/or increase the Gaussian width of the atomic contributions from large-distance neighbors, and rest assured that the contracted basis would provide a systematically-convergent description of this problem-adapted density. Incorporating a supervised component in the construction of the optimal basis is another possible

direction in which the numerical basis we introduce in this work can be developed further.

In the presence of multiple chemical elements, it is highly beneficial to construct a combined basis in which radial channels associated with different species are combined. This combined basis can capture the same amount of information of a primitive basis that is 3 to 5 times larger, and is essential to the efficient construction of high-order density correlation features. It shall help accelerate the convergence of the schemes, such as NICE, ACE, MTP, that rely on very high body order terms. We show that linear NICE models built on high-order combinations of the optimal basis yield much lower error than those constructed on a GTO basis of similar size, even though the truncation of the body order iteration, or introducing nonlinearities, can also affect, positively or negatively, convergence.

Given that the determination of the optimal basis is much less demanding than the fitting of even the simplest models, the fact it can be evaluated as rapidly of any other basis by using a spline approximation, and the fact that in all tests we performed led to comparable or better accuracy than standard choices of orthogonal bases, we recommend adopting this scheme in any machine-learning approach that requires representing an atomic density.

## ACKNOWLEDGMENTS

FM and MC acknowledge support by the NCCR MARVEL, funded by the Swiss National Science Foundation (SNSF). AG, SP and MC acknowledge support from the Swiss National Science Foundation (Project No. 200021-182057).

## REFERENCES

- <sup>1</sup>J. Behler, “Neural network potential-energy surfaces in chemistry: A tool for large-scale simulations,” *Phys. Chem. Chem. Phys.* **13**, 17930–55 (2011).
- <sup>2</sup>M. Rupp, A. Tkatchenko, K.-R. Müller, and O. A. von Lilienfeld, “Fast and Accurate Modeling of Molecular Atomization Energies with Machine Learning,” *Phys. Rev. Lett.* **108**, 058301 (2012).
- <sup>3</sup>A. P. Bartók, R. Kondor, and G. Csányi, “On representing chemical environments,” *Phys. Rev. B* **87**, 184115 (2013).
- <sup>4</sup>J. Behler and M. Parrinello, “Generalized Neural-Network Representation of High-Dimensional Potential-Energy Surfaces,” *Phys. Rev. Lett.* **98**, 146401 (2007).
- <sup>5</sup>B. J. Braams and J. M. Bowman, “Permutationally invariant potential energy surfaces in high dimensionality,” *Int. Rev. Phys. Chem.* **28**, 577–606 (2009).
- <sup>6</sup>A. V. Shapeev, “Moment Tensor Potentials: A Class of Systematically Improvable Interatomic Potentials,” *Multiscale Model. Simul.* **14**, 1153–1173 (2016).
- <sup>7</sup>A. Glielmo, P. Sollich, and A. De Vita, “Accurate interatomic force fields via machine learning with covariant kernels,” *Phys. Rev. B* **95**, 214302 (2017).
- <sup>8</sup>A. Grisafi, D. M. Wilkins, G. Csányi, and M. Ceriotti, “Symmetry-Adapted Machine Learning for Tensorial Properties of Atomistic Systems,” *Phys. Rev. Lett.* **120**, 036002 (2018).
- <sup>9</sup>B. Anderson, T. S. Hy, and R. Kondor, “Cormorant: Covariant Molecular Neural Networks,” in *NeurIPS* (2019) p. 10.
- <sup>10</sup>S. N. Pozdnyakov, M. J. Willatt, A. P. Bartók, C. Ortner, G. Csányi, and M. Ceriotti, “Incompleteness of Atomic Structure Representations,” *Phys. Rev. Lett.* **125**, 166001 (2020).
- <sup>11</sup>B. Onat, C. Ortner, and J. R. Kermode, “Sensitivity and dimensionality of atomic environment representations used for machine learning interatomic potentials,” *J. Chem. Phys.* **153**, 144106 (2020).
- <sup>12</sup>B. Parsaeifard, D. S. De, A. S. Christensen, F. A. Faber, E. Kocer, S. De, J. Behler, A. von Lilienfeld, and S. Goedecker, “An assessment of the structural resolution of various fingerprints commonly used in machine learning,” *Mach. Learn.: Sci. Technol.* (2020), 10.1088/2632-2153/abb212.
- <sup>13</sup>B. Huang and O. A. von Lilienfeld, “Communication: Understanding molecular representations in machine learning: The role of uniqueness and target similarity,” *The Journal of Chemical Physics* **145**, 161102 (2016).
- <sup>14</sup>F. Musil, A. Grisafi, A. P. Bartók, C. Ortner, G. Csányi, and M. Ceriotti, “Physics-inspired structural representations for molecules and materials,” *arxiv:2101.04673* (2021).
- <sup>15</sup>M. J. Willatt, F. Musil, and M. Ceriotti, “Feature optimization for atomistic machine learning yields a data-driven construction of the periodic table of the elements,” *Phys. Chem. Chem. Phys.* **20**, 29661–29668 (2018).
- <sup>16</sup>M. J. Willatt, F. Musil, and M. Ceriotti, “Atom-density representations for machine learning,” *J. Chem. Phys.* **150**, 154110 (2019).
- <sup>17</sup>J. Sanchez, F. Ducastelle, and D. Gratias, “Generalized cluster description of multicomponent systems,” *Physica A: Statistical Mechanics and its Applications* **128**, 334–350 (1984).
- <sup>18</sup>R. Drautz, “Atomic cluster expansion for accurate and transferable interatomic potentials,” *Phys. Rev. B* **99**, 014104 (2019).
- <sup>19</sup>A. Schäfer, H. Horn, and R. Ahlrichs, “Fully optimized contracted Gaussian basis sets for atoms Li to Kr,” *The Journal of Chemical Physics* **97**, 2571–2577 (1992).
- <sup>20</sup>V. Blum, R. Gehrke, F. Hanke, P. Havu, V. Havu, X. Ren, K. Reuter, and M. Scheffler, “Ab initio molecular simulations with numeric atom-centered orbitals,” *Comput. Phys. Commun.* **180**, 2175–2196 (2009).
- <sup>21</sup>F. Musil, M. Veit, A. Gosinski, G. Fraux, M. J. Willatt, M. Stricker, and M. Ceriotti, “Efficient implementation of atom-density representations,” *J. Chem. Phys.* **154**, 114109 (2021).
- <sup>22</sup>J. Nigam, S. Pozdnyakov, and M. Ceriotti, “Recursive evaluation and iterative contraction of  $N$ -body equivariant features,” *J. Chem. Phys.* **153**, 121101 (2020).
- <sup>23</sup>M. Bachmayr, G. Csányi, R. Drautz, G. Dussan, S. Etter, C. van der Oord, and C. Ortner, “Atomic cluster expansion: Completeness, efficiency and stability,” *arxiv:1911.03550* (2019).
- <sup>24</sup>B. K. Miller, M. Geiger, T. E. Smidt, and F. Noé, “Relevance of rotationally equivariant convolutions for predicting molecular properties,” *ArXiv Prepr. ArXiv200808461* (2020).
- <sup>25</sup>A. P. Bartók, J. Kermode, N. Bernstein, and G. Csányi, “Machine Learning a General-Purpose Interatomic Potential for Silicon,” *Phys. Rev. X* **8**, 041048 (2018), <https://link.aps.org/doi/10.1103/PhysRevX.8.041048>.
- <sup>26</sup>R. Ramakrishnan, P. O. Dral, M. Rupp, and O. A. von Lilienfeld, “Quantum chemistry structures and properties of 134 kilo molecules,” *Sci. Data* **1**, 1–7 (2014).
- <sup>27</sup>F. A. Faber, L. Hutchison, B. Huang, J. Gilmer, S. S. Schoenholz, G. E. Dahl, O. Vinyals, S. Kearnes, P. F. Riley, and O. A. von Lilienfeld, “Prediction Errors of Molecular Machine Learning Models Lower than Hybrid DFT Error,” *J. Chem. Theory Comput.* **13**, 5255–5264 (2017).
- <sup>28</sup>S. Pozdnyakov, “NICE libraries,” <https://github.com/cosmo-epfl/nice> (2020).
- <sup>29</sup>A. Gosinski, G. Fraux, G. Imbalzano, and M. Ceriotti, “The role of feature space in atomistic learning,” *Mach. Learn.: Sci.*

- Technol. **2**, 025028 (2021).
- <sup>30</sup>G. Imbalzano, A. Anelli, D. Giofr , S. Klees, J. Behler, and M. Ceriotti, “Automatic selection of atomic fingerprints and reference configurations for machine-learning potentials,” *J. Chem. Phys.* **148**, 241730 (2018).
- <sup>31</sup>Y. Eldar, M. Lindenbaum, M. Porat, and Y. Y. Zeevi, “The farthest point strategy for progressive image sampling,” *IEEE Trans. Image Process. Publ. IEEE Signal Process. Soc.* **6**, 1305–15 (1997).
- <sup>32</sup>M. Ceriotti, G. A. Tribello, and M. Parrinello, “Demonstrating the transferability and the descriptive power of sketch-map,” *J. Chem. Theory Comput.* **9**, 1521–1532 (2013).
- <sup>33</sup>A. P. Bart k, S. De, C. Poelking, N. Bernstein, J. R. Kermode, G. Cs nyi, and M. Ceriotti, “Machine learning unifies the modeling of materials and molecules,” *Sci. Adv.* **3**, e1701816 (2017).
- <sup>34</sup>M. A. Caro, “Optimizing many-body atomic descriptors for enhanced computational performance of machine learning based interatomic potentials,” *Phys. Rev. B* **100**, 024112 (2019).
- <sup>35</sup>S. de Jong and H. A. Kiers, “Principal covariates regression,” *Chemometrics and Intelligent Laboratory Systems* **14**, 155–164 (1992).
- <sup>36</sup>B. A. Helfrecht, R. K. Cersonsky, G. Fraux, and M. Ceriotti, “Structure-property maps with Kernel principal covariates regression,” *Mach. Learn.: Sci. Technol.* **1**, 045021 (2020).
- <sup>37</sup>R. K. Cersonsky, B. Helfrecht, E. A. Engel, S. Kliavinek, and M. Ceriotti, “Improving Sample and Feature Selection with Principal Covariates Regression,” *Mach. Learn.: Sci. Technol.* (2021), 10.1088/2632-2153/abfe7c.